communications physics

ARTICLE

https://doi.org/10.1038/s42005-023-01381-z OPEN

# Realization of non-Hermitian Hopf bundle matter

Yung Kim [1,2,7], Hee Chul Park [3,4,7], Minwook Kyung [1], Kyungmin Lee [1], Jung-Wan Ryu [3], Oubo You[5], Shuang Zhang [5], Bumki Min [1✉] & Moon Jip Park [3,6✉]

Non-trivial linking invariant encodes robust information of topological matter. It has been recently shown that the linking and winding of complex eigenenergy strings can classify one-dimensional non-Hermitian topological matter. However, in higher dimensions, bundles of linked strings can emerge such that every string is mutually linked with all the other strings. To the best of our knowledge, a non-Hermitian Hopf bundle has not been experimentally clarified. Here, we attempt to explore the non-Hermitian Hopf bundle by visualizing the global linking structure of spinor strings in the momentum space of a two-dimensional electric circuit. By exploiting the flexibility of reconfigurable couplings between circuit nodes, we study the non-Hermitian topological phase transition by exploring the intricate structure of the Hopf bundle. Furthermore, we find that the higher-order skin effect in real space is accompanied by the linking of spinor strings in momentum space, revealing bulk-boundary correspondence between the two domains.

[1] Department of Physics, Korea Advanced Institute of Science and Technology (KAIST), Daejeon 34141, Republic of Korea. [2] Department of Mechanical Engineering, Korea Advanced Institute of Science and Technology (KAIST), Daejeon 34141, Republic of Korea. [3] Center for Theoretical Physics of Complex Systems, Institute for Basic Science, Daejeon 34126, Republic of Korea. [4] Department of Physics, Pukyong National University, Busan 48513, Republic of Korea. [5] Department of Physics, University of Hong Kong, Hong Kong 999077, China. [6] Department of Physics, Hanyang University, Seoul 04763, Republic of Korea. [7] These authors contributed equally: Yung Kim, Hee Chul Park. ✉email: bmin@kaist.ac.kr; moonjippark@gmail.com

Studying the topological phases of matter that is protected by non-trivial linking and winding structure is an emerging area in the field of condensed matter physics[1–3]. Realizing such matters would bridge the gap between our knowledge of physics and the mathematical field of topology[4–24]. A recent interesting proposal utilizes the nature of the complex eigenenergy in non-Hermitian systems to show that one-dimensional systems described by complex eigenenergy strings can be classified by topological linking and winding invariants[25–32]. This non-Hermitian linking structure could therefore offer a promising approach for elucidating the robust physical quantity in the presence of open-environmental couplings[33–42]. Higher-dimensional systems, in general, tend to allow more intricate linking structures[43], but the experimental visualization and reconstruction of these linking structures are still lacking.

As a first step towards generalizing such linked-string matter, we introduce two-dimensional non-Hermitian electric circuit systems, whose Bloch Hamiltonian is described by the effective spinor representation. In situ control of the circuit network allows adiabatic deformations of the Hamiltonian (Fig. 1a). The adiabatic trajectory of equal spinors generally forms a line, which we refer to as spinor strings (SS). Such string representations of the non-Hermitian Hamiltonian are naturally characterized by the nontrivial topology that arises from the mutual linking of multiple strings. Mathematically, the bundle of SSs admits a linking structure, known as the Hopf bundle[44], in which each SS is linked to all the other strings.

While the Hopf bundle has been suggested as a tool for the topological comprehension of Hermitian systems[17,19], its influence on the boundary effects in non-Hermitian systems has yet to be determined. Here, we reveal an unusual type of bulk-boundary correspondence (BBC) associated with non-Hermitian Hopf bundles. It is shown that the nontrivial deformation of the Hamiltonian or the Hopf bundle, rather than the Hamiltonian itself, gives rise to the boundary states (or corner skin states). We demonstrate this in this work by employing a non-Hermitian electric circuit platform capable of exhibiting various Hopf bundle projections. Realizing such condensed phases of many linked strings would allow for the discovery of intricate non-Hermitian topological continuum.

## Results

**Non-Hermitian topological phases and Hopf bundle visualization**. We consider the generic deformable Hamiltonian of a two-dimensional non-Hermitian lattice consisting of unit cells with two sublattice sites,

$$H(\boldsymbol{k},\phi) = if_0(\boldsymbol{k},\phi)I_2 + f_x(\boldsymbol{k},\phi)\sigma_x + f_y(\boldsymbol{k},\phi)\sigma_y + f_z(\boldsymbol{k},\phi)\sigma_z, \tag{1}$$

where $\sigma$ represents the Pauli matrices for the sublattice degree of freedom and $\phi \in [0, 2\pi)$ is the periodic deformation parameter. The effective spinor $\boldsymbol{z}(\boldsymbol{k},\phi) = \left(\bar{f}_0 + i\bar{f}_x, \bar{f}_y + i\bar{f}_z\right)^T$ parameterizes the non-Hermitian Hamiltonian in Eq. (1) by

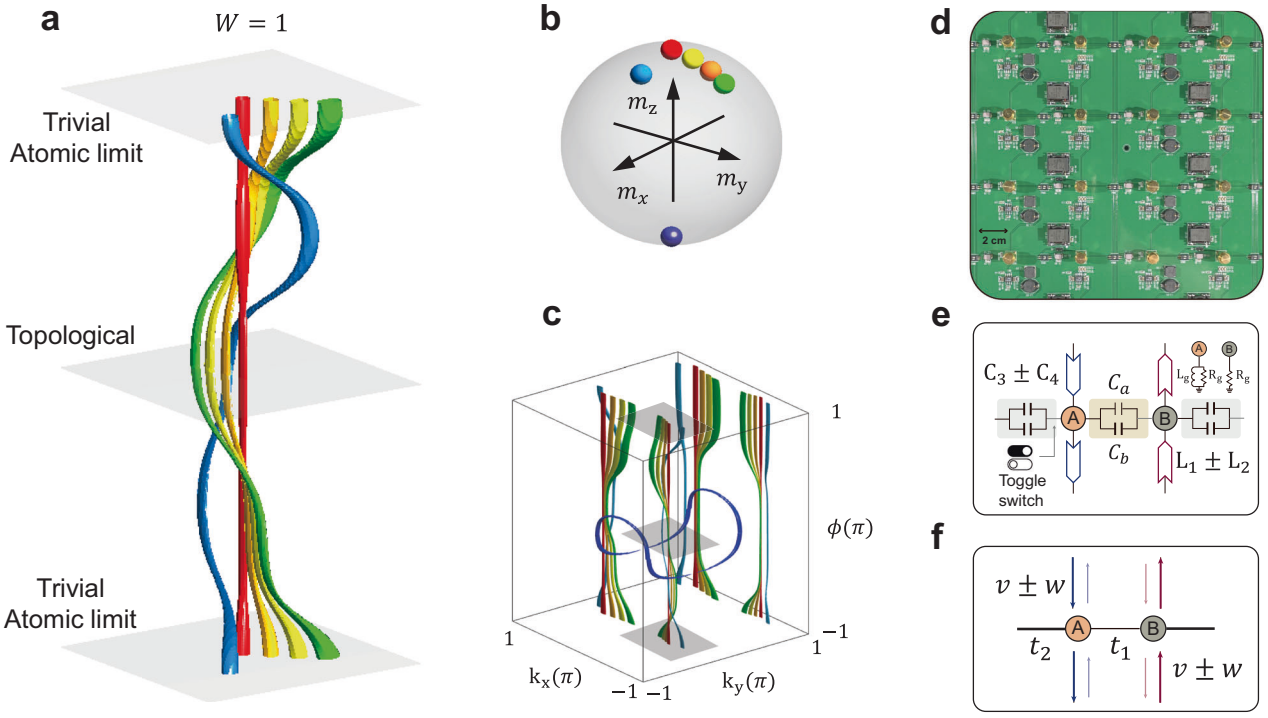


**Fig. 1 Non-Hermitian Hopf bundle and realization in circuit platform. a** Spinor strings (SSs) of the non-Hermitian Hopf bundle (linking number $W = 1$). The nontrivial Hopf bundle is characterized by mutual links between the SSs. The thickness of spinor strings is determined by the spinor distributions on Bloch sphere (**b**) Color map of different spinors projected onto the Bloch sphere. Each spinor represents the expectation values of the corresponding Bloch Hamiltonians. A certain range surrounding the selected expectation value is chosen to facilitate the visualization of spinor strings. The thickness of the spinor strings depicted in the figures corresponds to these ranges of expected values. **c** The spinor strings in the full Brillouin zone (Fig. 1a represents the shaded region). **d** Photographic image of the circuit network designed for the realization of Hopf bundle matter. **e** Layout of the unit cell consisting of circuit nodes A and B. Parallelly connected capacitors $\boldsymbol{C_a}$ and $\boldsymbol{C_b}$ are used to bridge the nodes, and toggle switches are used to selectively turn on/off the constituting capacitors along the effectively dimerized direction. To achieve anisotropic intercell coupling between unit cells in the *y*-direction, INICs with capacitors $\boldsymbol{C_3}$ and $\boldsymbol{C_4}$ and inductors $\boldsymbol{L_1}$ and $\boldsymbol{L_2}$ are employed to couple A-A and B-B nodes, respectively. **f** Tight-binding model of the unit cell. The red and blue arrows denote the staggered anisotropic hopping amplitudes $\boldsymbol{vw}$ between the unit cells along the *y*-direction. The shallow and bold lines denote intracell hopping $\boldsymbol{t_1}$ and intercell hopping $\boldsymbol{t_2}$, respectively.

encoding both information of the eigenstates and the finite lifetime arising from the non-Hermiticity. Furthermore, its spin expectation value $\boldsymbol{m}(\boldsymbol{k},\phi)=\boldsymbol{z}(\boldsymbol{k},\phi)^{\dagger}\boldsymbol{\sigma}\boldsymbol{z}(\boldsymbol{k},\phi)$ provides the visualization of the Hamiltonian projected from the momentum space onto the Bloch sphere ($S^2$) as shown in Fig. 1b. Under deformation, the trajectory of the spinors forms a line (SS) in the three-dimensional toric space $[(k_x,k_y,\phi)\in \mathrm{T}^3]$ (Fig. 1c). By counting the linking numbers between different SSs, the adiabatic deformations of the Hamiltonian can be topologically classified. The non-Hermitian Hopf bundle corresponds to nontrivial linking ($W=1$), and in general, the topological Hopf invariant $(\pi_{\mathrm{T}^3}(S^2)=\mathbb{Z})$ can be defined to count the linking number between different SSs,

$$W=\frac{1}{2\pi^2}\int \epsilon^{ijkl}\bar{f}_i d\bar{f}_j d\bar{f}_k d\bar{f}_l. \tag{2}$$

Here, $\epsilon^{ijkl}$ is the Levi-Civita symbol (see Supplementary Note 2 for a detailed calculation)[45]. We point out that the Hopf invariant in a non-Hermitian system is well-defined only in the two-band model, similar to the other delicate topological phases in Hermitian systems[46]. It is worth to note that, in general, the K-theoretical classification provides the relevant topological classification for multi-band models[26].

To exemplify this concept, we design and fabricate a two-dimensional circuit network (a square lattice of $8\times 8$) on a printed circuit board (PCB) (Fig. 1d), which allows us to design the deformable Hamiltonian in the momentum space. Specifically, the circuit is designed to achieve a Su–Schrieffer–Heeger (SSH) chain along the $x$-direction while emulating a Hatano-Nelson-like chain along the $y$-direction. The dimerized couplings along the $x$-direction mimic the SSH chain with intracell ($t_1$) and intercell ($t_2$) couplings, as depicted by the thin and thick black lines in Fig. 1f. The arrows indicate staggered directions of the nonreciprocal (asymmetric) couplings $v\pm w$ in the $y$-direction, with the colors of the arrows representing the sublattice sites (orange and gray for A and B sites, respectively). The Hamiltonian undergoes four characteristic configurations, depicted in Fig. 2a [second-order topological ($H_{\mathrm{SO}}$), first-order nonreciprocal ($H_{\mathrm{NR}}$), first-order dimerized phases ($H_{\mathrm{SSH}}$) and trivial atomic limit ($H_{\mathrm{triv}}$)], as a result of gradual adjustment of dimerization and nonreciprocity along the $x$- and $y$-directions. More specifically, we consider the adiabatic deformation of the Hamiltonian,

$$\begin{aligned}H(\boldsymbol{k},\phi)=&A(\phi)H_{\mathrm{SO}}(\boldsymbol{k})+B(\phi)H_{\mathrm{NR}}(\boldsymbol{k})+C(\phi)H_{\mathrm{triv}}(\boldsymbol{k})\\&+D(\phi)H_{\mathrm{SSH}}(\boldsymbol{k})\end{aligned} \tag{3}$$

where $A,B,C,D$ are the Gaussian-shaped deformation parameters shown in Fig. 2b (see Supplementary Note 2 for more detail). When the deformation consecutively encircles the four distinct Hamiltonian phases, the Hopf invariant corresponds to $W=1$ (i.e., the existence of the Hopf bundle, which is shown in Fig. 1a). In general, the change in the Hopf invariant is accompanied by the touching of distinct SSs, where the SSs become ill-defined (i.e., vanishing of the Bloch Hamiltonian).

In the circuit implementation (Fig. 1e), the two sublattices within each unit cell are represented by Circuit Nodes A and B. Along the effectively dimerized direction, the intracell and intercell couplings are made switchable by combining toggle switches in tandem with the parallelly connected capacitors $C_a$ and $C_b$. To observe the Hamiltonian deformation, we can individually vary the intracell and intercell couplings (characterized by effective capacitances $C_1$ and $C_2$) by selectively activating the relevant capacitor in the branch. The negative impedance

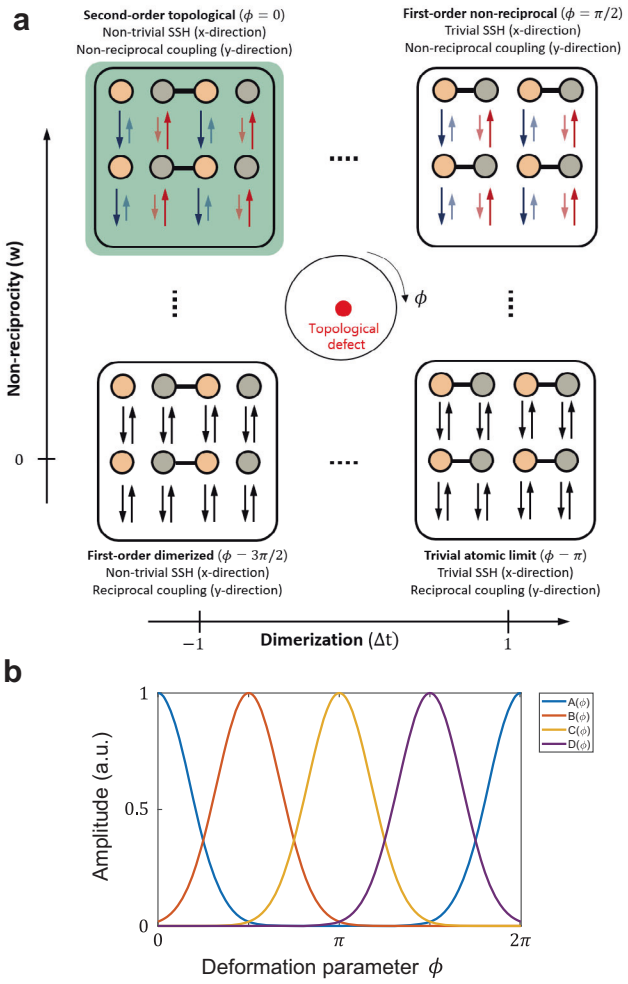


**Fig. 2 Adiabatic deformation scheme of the system. a** Adiabatic deformation scheme of the Hamiltonian and the four distinct phases of the Hamiltonian configurations. Red, blue and black arrows indicate the nonreciprocal (red and blue) and reciprocal (black) couplings along the $y$-direction. Black horizontal couplings represent the SSH-like coupling along the $x$-direction. For instance, the two-dimensional slice at deformation parameter $\phi=0$ represents the topologically nontrivial Hamiltonian, while the slice at $\phi=\pi$ represents the vacuum Hamiltonian outside the circuit. The first-order nonreciprocal ($\phi=\pi/2$) and the first-order dimerized phases ($\phi=3\pi/2$) correspond to the Hamiltonians where the $x$- and $y$-directional hoppings are, respectively trivialized. The skin states as a topological defect (drawn with a red dot) are guaranteed to exist by the presence of the Hopf bundle. **b** Plot of the Gaussian-shaped deformation parameters. See Supplementary Note 2 for detail information.

converters through current inversion (INIC)[47,48] are positioned in the branch between unit cells with alternating orientations to achieve the required staggered pattern of nonreciprocal couplings along the $y$-direction. More specifically, INICs configured with Capacitors $C_3$ and $C_4$ are used to provide nonreciprocal coupling between the A nodes along the $y$-direction, while INICs with Inductors $L_1$ and $L_2$ are placed in the branch between the B nodes (see Supplementary Note 1 and Fig. S1 for the comprehensive circuit layout). Furthermore, an inductor $L_g$ is added to match the resonance condition by connecting Node A to the ground, and a resistor $R_g$ is employed in the measurement for impedance matching. At resonance, the (scaled) circuit Laplacian derived from the fabricated platform takes the form of the above tight-

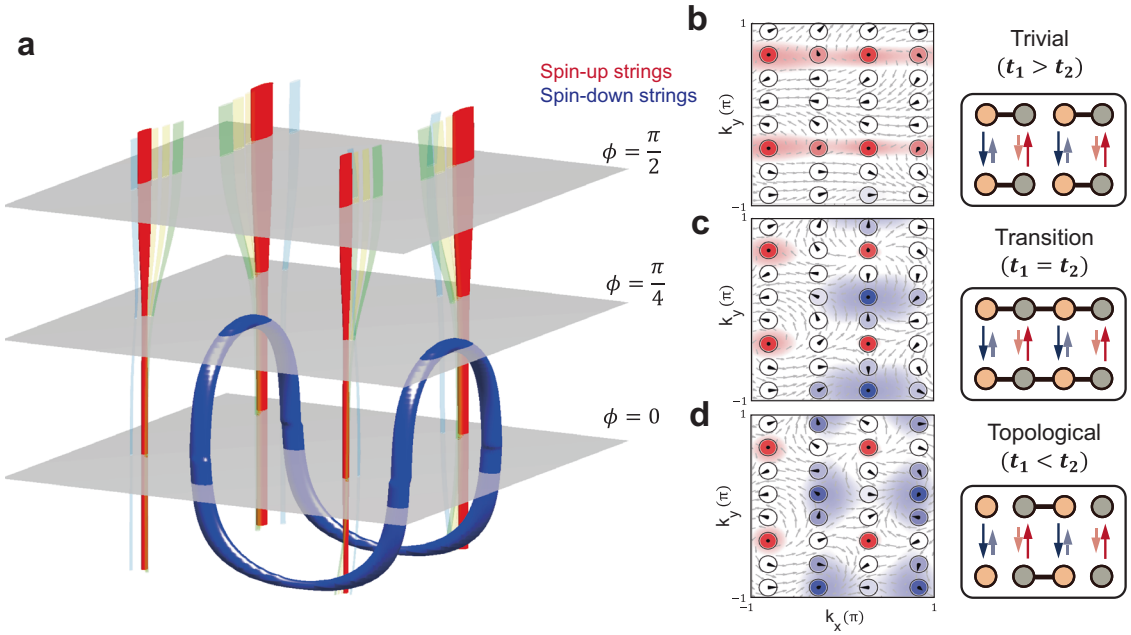


**Fig. 3 Sectional visualization of the Hopf bundle. a** Theoretically calculated adiabatic deformation of the spinor strings. The red and blue strings represent the spin-up and the spin-down spinors, respectively. **b**–**d** Experimentally observed sectional visualization of the deformation, corresponding to periodic deformation parameter $\phi = \frac{\pi}{2}, \frac{\pi}{4}$ and 0, respectively. The two-dimensional slice of the Hopf bundle in the first-order nonreciprocal phase shows only the spin-up SSs (**b**). The appearance points of the spin-down states start to be detached at the topological phase transition (**c**). In the second-order topological phase, one of the four points of each SS is trapped inside the other four points of the other SSs (**d**).

binding Hamiltonian (see Supplementary Note 1),

$$(i\omega_0)^{-1} J(\boldsymbol{k},\omega_0) = \left(-2iC_4 \sin k_y\right) I_2 + \left(C_1 + C_2 \cos k_x\right)\sigma_x + \left(-C_2 \sin k_x\right)\sigma_y + \left(-2C_3 \cos k_y\right)\sigma_z \quad (4)$$

where $\omega_0$ is the resonance frequency of $LC$ resonators ($\omega_0 = 1/\sqrt{L_1 C_3} = 1/\sqrt{L_2 C_4}$). There is a one-to-one correspondence between the tight-binding model and the circuit lattice, which can be established by equating the coupling coefficients to the capacitances in the circuit: $t_1 = C_1$, $t_2 = C_2$, $v = -C_3$, $w = C_4$ (see Supplementary Note 1).

Our circuit configuration features switchable couplings, which serve as an example of in situ Hamiltonian (or Laplacian) deformations. To achieve this, we set the toggle switches in such a way that the three phases shown in Fig. 3 can be accessed in a single electric lattice. Specifically, the nontrivial, critical, and trivial phases of SSH chains are prepared by setting the normalized coupling difference $\triangle t = (t_1 - t_2)/(t_1 + t_2)$ to $-1$, 0, and 1, respectively. By controlling the relative strengths of intracellular and intercellular couplings, we sectionally visualize the Hopf bundle with Hamiltonian deformation from the second-order topological to the first-order nonreciprocal phase (see Fig. 2a). Experimentally measured spinor configurations agree well with the theoretical predictions of the deformations (Fig. 3a). More specifically, we track the trajectories of the spin-up spinors (red dots) and the spin-down spinors (blue dots). The spin-up spinors and the spin-down spinors form quadruplet distributions in the second-order topological phase (Fig. 3d). As the intracell and intercell couplings are gradually matched ($\triangle t = 0$), the system approaches the first-order nonreciprocal phase. The spin-down states merge and pair-annihilate (Fig. 3c). Eventually, only the spin-up SSs are observed in the momentum space without any signature of their linking with the spin-down SSs (Fig. 3b), featuring the onset of the trivial atomic limit.

**Bulk-boundary correspondence of non-Hermitian Hopf bundle**. We simultaneously measure complex admittance spectra and modal voltage distributions in real space (Fig. 4a–k). To reconstruct the circuit Laplacian under the periodic boundary condition (PBC) and open boundary condition (OBC), a series of current-voltage measurements are carried out with the corresponding boundary conditions by adjusting both the bulk and the boundary hopping elements. The comparison of Fig. 4d, h clearly shows the qualitative difference between the PBC and OBC spectra in the second-order topological phase ($\triangle t$<0). Furthermore, we find the appearance of in-gap states (represented by red data points), which are identified as non-Hermitian skin defect states, as will be explained further below[49–60]. Since the intracell and intercell couplings are gradually matched ($\triangle t = 0$), the line gap closes ($\mathrm{Im}[j] = 0$, see Fig. 4c), which coincides with the topological phase transitions between the second-order topological and first-order nonreciprocal phases. In the nonreciprocal trivial phase, the measured bulk spectrum exhibits the reoccurrence of the line gap in the complex energy plane (see Supplementary Note 3, 4 for the detailed spectral analysis)[26]. Correspondingly, we observe the absorption of the in-gap states to the bulk (represented by the navy dots in the OBC spectra in Fig. 4).

The in-gap states are distinguished from the other extended bulk states by the localizations at the corner (Fig. 4k). This localization is similar to the phenomena of the second-order Hermitian topological phases[61]. However, we find that the number of localized states at the corners scale with the length of the system, which is in direct contrast with the phenomenology of the Hermitian topological phases. The anomalous scaling is indicative of the macroscopic collapse of the bulk state behavior known as the second-order non-Hermitian skin effect (NHSE)[62–66]. The emergence of the corner skin states can be naturally explained within the framework of the topological defect[26,62,67]. We consider the gradual variation of the system Hamiltonian in the second-order topological phase as a function

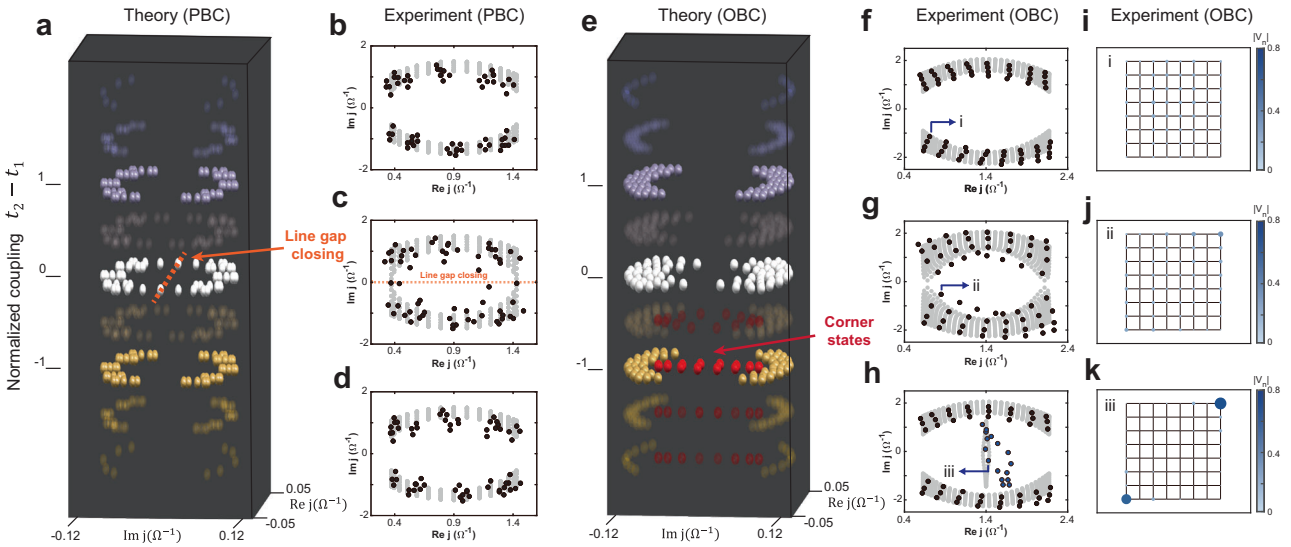


**Fig. 4 Complex admittance spectra and modal voltage distributions.** Theoretically calculated and experimentally measured complex admittance spectra, and modal voltage distributions under PBC (**a**–**d**) and OBC (**e**–**k**). In the nonreciprocal trivial phase (**b**, **f**), only the two bulk bands are observed in the PBC and OBC spectra. At the second-order topological phase transition, the line gap of the non-Hermitian Hamiltonian closes (**c**, **g**). The experimentally measured PBC spectrum clearly shows the line gap touching the topological phase transition (**c**). Correspondingly, we observe the lifting of in-gap states from the bulk in the OBC spectrum (**g**). In the second-order topological phase, modal voltage distributions confirm 16 in-gap states within the line gap (**h**). The in-gap states exhibit the localized modal voltage distribution at the corner (**k**), which is in direct contrast with the other extended bulk states (**i**, **j**). The black dots in the complex admittance spectra denote the measured data, while the background gray dots are the calculated data. In the modal plot, the eigenvoltage amplitude is plotted with the size and color of the circle.

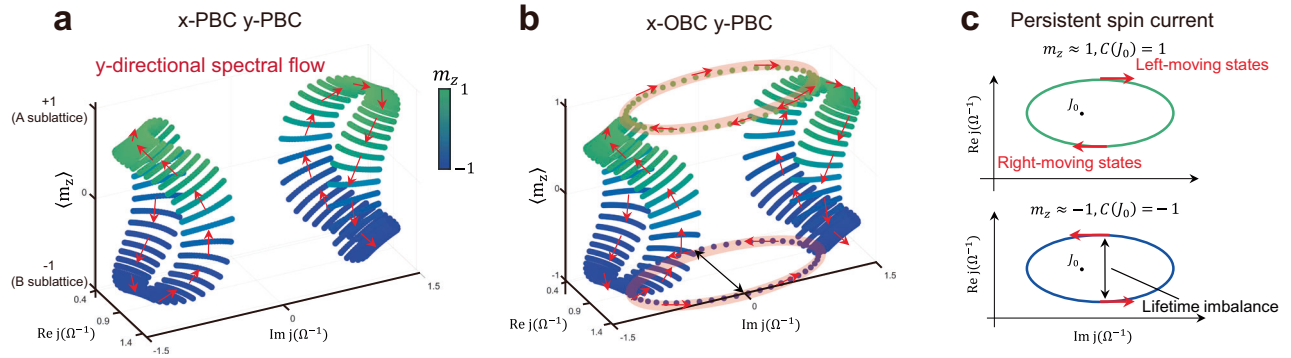


**Fig. 5 Complex energy spectra and corner skin states in OBC.** Complex energy spectra of the eigenstates as a function of the spinor polarization $\boldsymbol{m_z}$: (**a**) PBC in both the *x*- and *y*-directions, (**b**) OBC for the x-direction and PBC for the *y*-direction. The colors green and blue indicate the spinor polarization amplitude. Red arrows represent the spectral flow of the eigenstates as a function of the momentum $\boldsymbol{k_y}$. The highlighted red circles are the two in-gap bands that appear at maximum polarization ($\boldsymbol{m_z}1$). **c** The spectral flow of the ring states results in a lifetime imbalance between the left- and right-moving states, which manifests as the non-Hermitian skin effect under the OBC for both the *x*- and *y*-directions.

of the real space position $\mathbf{r} = (R \sin \phi, R \cos \phi)$; here, $\mathbf{r}$ is defined on the loop surrounding the corner. For instance, $\phi = 0$ represents the bulk Hamiltonian inside the circuit, while $\phi = \pi$ is the vacuum Hamiltonian outside the circuit. This variation explicitly mirrors the adiabatic deformation in Fig. 2. The existence of the topological defect within the loop manifests as the corner skin state.

The microscopic origin of the BBC can be inferred by analysing the spectral flow of the complex energy bands. Figure 5 shows the complex energy band with a nontrivial Hopf invariant plotted as a function of the spin polarization $m_z$. While two complex energy bands are separated by the imaginary gap under the PBC, their $k_y$-directional spectral flows (drawn with red arrows) exhibit opposite winding directions in the $m_z - \mathrm{Re}[j]$ plane (see Fig. 5a). When the OBC is imposed in the *x*-direction (Fig. 5b), two in-gap bands (highlighted by red circles) additionally appear with maximal polarizations ($m_z \approx \pm 1$). The opposite polarizations indicate that the ring states originate at the SSH boundaries and are localized at the x-directional ends. Each ring state results in the counter-directional spectral flow, characterized by the opposite winding number $C(J)$ defined in the $\mathrm{Re}[j] - \mathrm{Im}[j]$ plane[27], i.e.,

$$C(J_0) = \frac{1}{2\pi i} \int dk_y \partial_{k_y} \log\left(j\left(k_y\right) - J_0\right), \tag{5}$$

where $j\left(k_y\right)$ is the admittance spectra of the ring states and $J_0 \in \mathbb{C}$ is the reference complex admittance. The nontrivial winding number, $C\left(J_0\right)$, of the ring state spectrum ensures a finite lifetime ($\propto \mathrm{Re}[j]$) imbalance between the left ($v_g < 0$) and right moving ($v_g > 0$) states, where $v_g \propto \frac{\partial \mathrm{Im} j}{\partial k_y}$ denotes the group velocity (Fig. 5c). As a result, the direction of the persistent current along the two

edges of SSH chains becomes opposite. When the OBC is further imposed in the $y$-direction, the persistent current leads to macroscopic accumulations of ring states at the corner of the system. Finally, we highlight the distinction between the topological protection in the second-order NHSE and previously reported works. Kawabata et al.[62] have shown that $C_4$-rotational symmetry protects the second-order skin effect (see Supplementary Note 2 for connection with our model). In contrast, the Hopf invariant in our model requires no additional spatial symmetry, and it is a well-defined topological invariant in the two-band model. Nevertheless, we point out that the addition of a trivial band may trivialize the Hopf invariant because the homotopy group is well-defined only in the two-band model.

## Discussions

In this work, we have successfully realized a non-Hermitian Hopf bundle and mapped out the linking structure of SSs using an electric circuit lattice. The asymmetric couplings in real space are found to be crucial for achieving the non-Hermitian Hopf bundle structure in momentum space. The effective capacitance switching capability in the measurement allows three-dimensional visualization of the nontrivial linking of SSs as well as the identification of the topological phase transition by in situ Hamiltonian deformation. Using this methodology, the BBC between the non-Hermitian Hopf bundle of the bulk and the defect states at the corner is uncovered. We expect that the proposed non-Hermitian Hopf bundle platform and the visualization technique of its linking structure will serve as an intriguing testbed for the investigation and classification of non-Hermitian topology. It is noteworthy that the circuit platform enables the design of long-range nonreciprocal couplings, which may lead to the realization of Hopf bundles with higher linking numbers. In theory, new kinds of skin states would appear at the interface between two Hopf bundles with different linking numbers, wherein multiple localization length scales would coexist. Consequently, the generalization of higher-number linking structures in a non-Hermitian Hopf bundle would be an intriguing subject for future research.

## Methods

**Sample fabrication**. We fabricate a two-dimensional circuit network consisting of $8 \times 8$ unit cells on a PCB. In the $x$-direction, we parallelly connect two different types of capacitors with a toggle switch in each branch: $C_a = 47$ nF (WALSIN) and $C_b = 94$ nF (KEMET). Using the toggle switch, we can choose between the capacitance values of 47 nF, 94 nF, and 141 nF. As shown in Fig. 1e, we use INICs to achieve asymmetric couplings in the $y$-direction; in branches connecting A nodes, operational amplifiers (Analog Devices) are configured with capacitors of $C_3 = 47$ nF and $C_4 = 94$ nF (WALSIN), while those in branches connecting B nodes contain inductors of $L_1 = 150$ μH (BOURNS) and $L_2 = 75$ μH (Abracon). In addition, a capacitor with a value of $C_s = 4700$ nF and a resistor with a value of $R_s = 20$ Ω are incorporated in the INICs to stabilize the circuit. To satisfy the resonance condition of the LC resonator, Node A is grounded by an inductor of $L_g = 18.7$ μH. For impedance matching, each node is additionally grounded by a resistor $R_g = 20$ Ω. At each node, 50-Ω SMA connectors are installed for voltage measurement.

**Experimental implementation**. The circuit Laplacian can be reconstructed by measuring the input-current and output-voltage response[68]. The measurement is conducted at the resonance frequency of $f = 60$ kHz. The AC current is inputted into the circuit by the function generator (GWinstek). We then measured the response at all nodes by using data acquisition (DAQ, National Instruments). Circuit Laplacian reconstruction can be accomplished through a series of measurement protocols with appropriate boundary conditions[47]. Under the OBC, we feed an input current at a specific node and measure the output voltage at all the other nodes. This procedure continues until all nodes in the circuit are set as an input. Under the PBC, we feed an input current at specific sublattices A and B and measure the corresponding voltage responses.

## Data availability

All data supporting the plots presented in this paper can be made available upon reasonable request to the corresponding author.

## Code availability

The code used to analyse the data can be made available upon reasonable request to the corresponding author.

Received: 4 April 2023; Accepted: 8 September 2023;
Published online: 27 September 2023

## References

1. Kitaev, A. Anyons in an exactly solved model and beyond. *Ann. Phys.* **321**, 2 (2006).
2. Levin, M. A. & Wen, X.-G. String-net condensation: a physical mechanism for topological phases. *Phys. Rev. B* **71**, 045110 (2005).
3. Fang, C., Weng, H., Dai, X. & Fang, Z. Topological nodal line semimetals. *Chin. Phys. B* **25**, 117106 (2016).
4. Lee, C. H. et al. Imaging nodal knots in momentum space through topolectrical circuits. *Nat. Commun.* **11**, 4385 (2020).
5. Hu, H. & Zhao, E. Knots and non-Hermitian Bloch bands. *Phys. Rev. Lett.* **126**, 010401 (2021).
6. Ezawa, M. Topological semimetals carrying arbitrary Hopf numbers: Fermi surface topologies of a Hopf link, Solomon's knot, trefoil knot, and other linked nodal varieties. *Phys. Rev. B* **96**, 041202 (2017).
7. Patil, Y. S. S. et al. Measuring the knot of non-Hermitian degeneracies and non-commuting braids. *Nature* **607**, 271 (2022).
8. Belopolski, I. et al. Observation of a linked-loop quantum state in a topological magnet. *Nature* **604**, 647 (2022).
9. Bi, R., Yan, Z., Lu, L. & Wang, Z. Nodal-knot semimetals. *Phys. Rev. B* **96**, 201305 (2017).
10. Ahn, J., Kim, D., Kim, Y. & Yang, B.-J. Band topology and linking structure of nodal line semimetals with Z2 monopole charges. *Phys. Rev. Lett.* **121**, 106403 (2018).
11. Yan, Z. et al. Nodal-link semimetals. *Phys. Rev. B* **96**, 041103 (2017).
12. Chang, G. et al. Topological Hopf and chain link semimetal states and their application to Co2MnGa. *Phys. Rev. Lett.* **119**, 156401 (2017).
13. Kienzle, E. & Rayan, S. Hyperbolic band theory through Higgs bundles. *Adv. Math.* **409**, 108664 (2022).
14. Deng, D.-L., Wang, S.-T., Sun, K. & Duan, L.-M. Probe knots and Hopf insulators with ultracold atoms. *Chin. Phys. Lett.* **35**, 013701 (2017).
15. Zhou, Y., Xiong, F., Wan, X. & An, J. Hopf-link topological nodal-loop semimetals. *Phys. Rev. B* **97**, 155140 (2018).
16. Schuster, T. et al. Realizing Hopf insulators in dipolar spin systems. *Phys. Rev. Lett.* **127**, 015301 (2021).
17. Sugic, D. et al. Particle like topologies in light. *Nat. Commun.* **12**, 6785 (2021).
18. Kong, L.-J. et al. High capacity topological coding based on nested vortex knots and links. *Nat. Commun.* **13**, 2705 (2022).
19. Wan, C. et al. Scalar optical hopfions. *eLight* **2**, 22 (2022).
20. Tkalec, U., Ravnik, M., Čopar, S., Žumer, S. & Muševič, I. Reconfigurable knots and links in chiral nematic colloids. *Science* **333**, 62–65 (2011).
21. Wang, K., Xiao, L., Budich, J. C., Yi, W. & Xue, P. Simulating exceptional non-hermitian metals with single-photon interferometry. *Phys. Rev. Lett.* **127**, 026404 (2021).
22. Chen, T. et al. Creation of electrical knots and observation of DNA topology. *N. J. Phys.* **23**, 093045 (2021).
23. Liu, G. G. et al. Topological chern vectors in three-dimensional photonic crystals. *Nature* **609**, 925–930 (2022).
24. Yu, Y. et al. Experimental unsupervised learning of non-Hermitian knotted phases with solid-state spins. *npj Quantum Inf.* **8**, 116 (2022).
25. Wang, K., Dutt, A., Wojcik, C. C. & Fan, S. Topological complex-energy braiding of non-Hermitian bands. *Nature* **598**, 59 (2021).

26. Kawabata, K., Shiozaki, K., Ueda, M. & Sato, M. Symmetry and topology in non-Hermitian physics. *Phys. Rev. X* **9**, 041015 (2019).
27. Okuma, N., Kawabata, K., Shiozaki, K. & Sato, M. Topological origin of non-Hermitian skin effects. *Phys. Rev. Lett.* **124**, 086801 (2020).
28. Zhang, X. et al. Tidal surface states as fingerprints of non-Hermitian nodal knot metals. *Commun. Phys.* **4**, 47 (2021).
29. Ghatak, A., Brandenbourger, M., van Wezel, J. & Coulais, C. Observation of non-Hermitian topology and its bulk–edge correspondence in an active mechanical metamaterial. *Proc. Natl. Acad. Sci.* **117**, 29561 (2020).
30. Wang, K. et al. Generating arbitrary topological windings of a non-Hermitian band. *Science* **371**, 1240 (2021).
31. Zhang, L. et al. Acoustic non-Hermitian skin effect from twisted winding topology. *Nat. Commun.* **12**, 6297 (2021).
32. Wang, K. et al. Detecting non-Bloch topological invariants in quantum dynamics. *Phys. Rev. Lett.* **127**, 270602 (2021).
33. Rotter, I. A non-Hermitian Hamilton operator and the physics of open quantum systems. *J. Phys. A: Math. Theor.* **42**, 153001 (2009).
34. El-Ganainy, R. et al. Non-Hermitian physics and PT symmetry. *Nat. Phys.* **14**, 11 (2018).
35. Sun, X.-Q., Zhu, P. & Hughes, T. L. Geometric response and disclination-induced skin effects in non-Hermitian systems. *Phys. Rev. Lett.* **127**, 066401 (2021).
36. Sun, X.-Q., Wojcik, C. C., Fan, S. & Bzdušek, T. C. V. Alice strings in non-Hermitian systems. *Phys. Rev. Res.* **2**, 023226 (2020).
37. Hu, H., Sun, S. & Chen, S. Knot topology of exceptional point and non-Hermitian no-go theorem. *Phys. Rev. Res.* **4**, L022064 (2022).
38. Wojcik, C. C., Wang, K., Dutt, A., Zhong, J. & Fan, S. Eigenvalue topology of non-Hermitian band structures in two and three dimensions. *Phys. Rev. B* **106**, L161401 (2022).
39. Su, R. et al. Direct measurement of a non-Hermitian topological invariant in a hybrid light-matter system. *Sci. Adv.* **7**, eabj8905 (2021).
40. Yang, Z. & Hu, J. Non-Hermitian Hopf-link exceptional line semimetals. *Phys. Rev. B* **99**, 081102 (2019).
41. Tang, W., Ding, K. & Ma, G. Direct measurement of topological properties of an exceptional parabola. *Phys. Rev. Lett.* **127**, 034301 (2021).
42. Weidemann, S., Kremer, M., Longhi, S. & Szameit, A. Topological triple phase transition in non-Hermitian Floquet quasicrystals. *Nature* **601**, 354 (2022).
43. Adams, J. F. & Atiyah, M. F. K-theory and the Hopf invariant. *Q. J. Math.* **17**, 31 (1966).
44. Mosseri, R. & Dandoloff, R. Geometry of entangled states, Bloch spheres and Hopf fibrations. *J. Phys. A: Math. Gen.* **34**, 10243 (2001).
45. Ren, J.-R., Li, R. & Duan, Y.-S. Inner topological structure of Hopf invariant. *J. Math. Phys.* **48**, 073502 (2007).
46. Moore, J. E., Ran, Y. & Wen, X. G. Topological surface states in three-dimensional magnetic insulators. *Phys. Rev. Lett.* **101**, 186805 (2008).
47. Helbig, T. et al. Band structure engineering and reconstruction in electric circuit networks. *Phys. Rev. B* **99**, 161114 (2019).
48. Helbig, T. et al. Generalized bulk–boundary correspondence in non-Hermitian topolectrical circuits. *Nat. Phys.* **16**, 747 (2020).
49. Yao, S. & Wang, Z. Edge states and topological invariants of non-Hermitian systems. *Phys. Rev. Lett.* **121**, 086803 (2018).
50. Song, F., Yao, S. & Wang, Z. Non-Hermitian topological invariants in real space. *Phys. Rev. Lett.* **123**, 246801 (2019).
51. Claes, J. & Hughes, T. L. Skin effect and winding number in disordered non-Hermitian systems. *Phys. Rev. B* **103**, L140201 (2021).
52. Jiang, H., Lang, L.-J., Yang, C., Zhu, S.-L. & Chen, S. Interplay of non-Hermitian skin effects and Anderson localization in nonreciprocal quasiperiodic lattices. *Phys. Rev. B* **100**, 054301 (2019).
53. Longhi, S. Spectral deformations in non-Hermitian lattices with disorder and skin effect: a solvable model. *Phys. Rev. B* **103**, 144202 (2021).
54. Gong, Z. et al. Topological phases of non-Hermitian systems. *Phys. Rev. X* **8**, 031079 (2018).
55. Zhang, K., Yang, Z. & Fang, C. Correspondence between winding numbers and skin modes in non-Hermitian systems. *Phys. Rev. Lett.* **125**, 126402 (2020).
56. Yang, Z., Zhang, K., Fang, C. & Hu, J. Non-Hermitian bulk-boundary correspondence and auxiliary generalized Brillouin zone theory. *Phys. Rev. Lett.* **125**, 226402 (2020).
57. Yi, Y. & Yang, Z. Non-Hermitian skin modes induced by on-site dissipations and chiral tunneling effect. *Phys. Rev. Lett.* **125**, 186802 (2020).
58. Borgnia, D. S., Kruchkov, A. J. & Slager, R.-J. Non-Hermitian boundary modes and topology. *Phys. Rev. Lett.* **124**, 056802 (2020).
59. Zhang, K., Yang, Z. & Fang, C. Universal non-Hermitian skin effect in two and higher dimensions. *Nat. Commun.* **13**, 2496 (2022).
60. Liu, S. et al. Non-Hermitian skin effect in a non-Hermitian electrical circuit. *Research* **2021**, 5608038 (2021).
61. Benalcazar, W. A., Bernevig, B. A. & Hughes, T. L. Quantized electric multipole insulators. *Science* **357**, 61 (2017).
62. Kawabata, K., Sato, M. & Shiozaki, K. Higher-order non-Hermitian skin effect. *Phys. Rev. B* **102**, 205118 (2020).
63. Okugawa, R., Takahashi, R. & Yokomizo, K. Second-order topological non-Hermitian skin effects. *Phys. Rev. B* **102**, 241202 (2020).
64. Fu, Y., Hu, J. & Wan, S. Non-Hermitian second-order skin and topological modes. *Phys. Rev. B* **103**, 045420 (2021).
65. Shang, C. et al. Experimental identification of the second-order non-Hermitian skin effect with physics-graph-informed machine learning. *Adv. Sci.* **9**, 2202922 (2022).
66. Zou, D. et al. Observation of hybrid higher-order skin-topological effect in non-Hermitian topolectrical circuits. *Nat. Commun.* **12**, 7201 (2021).
67. Teo, J. C. Y. & Kane, C. L. Topological defects and gapless modes in insulators and superconductors. *Phys. Rev. B* **82**, 115120 (2010).
68. Lee, C. H. et al. Topolectrical circuits. *Commun. Phys.* **1**, 39 (2018).


## Acknowledgements

This work was supported by National Research Foundation of Korea (NRF) through the government of Korea (NRF- 2022R1A2C301335311). This work was also supported by the center for Advanced Meta-Materials (CAMM) funded by Korea Government (MSIP) as Global Frontier Project (NRF-2014M3A6B306370934). M.J.P., J.-W.R. and H.C.P. acknowledge financial support from the Institute for Basic Science in the Republic of Korea through the project IBS-R024-D1.

## Author contributions

Y.K., H.C.P., B.M. and M.J.P. conceptualized the project. Y.K., M.K. and K.L. carried out the circuit experiments and data analysis; H.C.P., J.-W.R. and M.J.P. developed the theoretical analysis. O.Y. and S.Z. participated in the analysis of all results. B.M. and M.J.P. supervised the project. The manuscript reflects the contributions of all authors.

## Competing interests

The authors declare no competing interests.

## Additional information

**Supplementary information** The online version contains supplementary material available at https://doi.org/10.1038/s42005-023-01381-z.

**Correspondence** and requests for materials should be addressed to Bumki Min or Moon Jip Park.

**Peer review information** *Communications Physics* thanks the anonymous reviewers for their contribution to the peer review of this work. A peer review file is available.